Chemical Science

ROYAL SOCIETY OF CHEMISTRY

EDGE ARTICLE

View Article Online
View Journal | View Issue

Cite this: *Chem. Sci.*, 2025, **16**, 20990

All publication charges for this article have been paid for by the Royal Society of Chemistry

Ultra-stable aqueous electrochromism based on $[EMIM]^+/I_3^-$ coordination

Fengjiao Meng,†[a] Junsen Zhong,†[a] Xiaoqian Tan,[a] Jianbo Cheng,[b] Bo Xiao,*[b] Shengliang Zhang,[c] Fuyi Jiang,*[a] Wenbao Liu,[a] Wei Liu[a] and Litao Kang*[a]

Received 28th June 2025
Accepted 25th September 2025

DOI: 10.1039/d5sc04767f

rsc.li/chemical-science

Electrochromic (EC) windows are receiving extensive attention owing to their flexibly adjustable optical properties controlled by external bias. Nevertheless, the widespread commercialization of EC windows still faces substantial impediments, including high cost, intricate fabrication processes, slow switching times and especially poor durability. Herein, we propose a facile yet high-performance EC system based on the reversible electrodeposition of iodine, which is theoretically free of "ion-trapping", structure degradation, dendrite growth and corrosion issues encountered by the traditional EC windows. To overcome the polyiodide shuttling problem, the electrolyte is further modified with $[EMIM]^+$, which can coordinate with the polyiodide intermediates to form insoluble $[EMIM]I_3$, and thereby effectively suppress polyiodide formation and shuttling. Moreover, the preferential adsorption of $[EMIM]^+$ onto the Zn counter electrode ensures uniform and stable Zn deposition/stripping, synergistically improving the durability of the I_2–Zn EC window. With these multifaceted merits, the simple EC system simultaneously achieves rapid response speeds ($t_{coloring}$: 7 s, $t_{bleaching}$: 6 s), high optical modulation amplitude (89.6% at 500 nm), impressive coloration efficiency (44.8 cm^2 C^{-1}) and excellent lifetime (without performance attenuation after 10 000 cycles). The scaling potential of the system is further demonstrated by constructing a large-area (10 × 10 cm^2) device.

1. Introduction

Nowadays, the energy consumption in buildings' heating, ventilation, and air conditioning systems accounts for more than 25% of the total energy consumption in the world.[1] Electrochromic (EC) windows can effectively improve buildings' energy efficiency and living comfort, by means of adapting the ambient temperature and initiating solar irradiation changes with their controllable transmittances.[2] A classic EC window features a sandwich-structure consisting of an EC film, an ion-storage (IS) film, and an electrolyte layer sandwiched by the EC and IS films.[3] The EC film, as the core functional component, to a large extent determines the optical properties and durability of the device.[4] Therefore, the rational design of the EC film is vitally important for the establishment of a high-performance EC window. The implementation of conventional ion insertion/extraction-type EC films requires pre-coating of the EC materials (*e.g.*, WO_3,[5,6] V_2O_5,[7] TiO_2,[8] PB[9]) onto transparent conductive substrates. To ensure high EC performance, the structures of the EC films, including thickness, porosity, uniformity, and phase composition, should be stringently controlled.[10] Inevitably, the prevalent approaches involve complex and energy-intensive preparation processes to achieve high-quality EC films, significantly raising fabrication costs while limiting the production yield and reliability.[11] Furthermore, a considerable proportion of the ion insertion/extraction EC films suffer from inferior lifetimes because of "ion-trapping" and structure degradation.[12,13]

Alternatively, EC abilities can also be achieved *via* reversible metal electrodeposition/dissolution reactions (*e.g.*, Bi,[14] Cu,[15] Ag[16] and Zn[17]), which in theory can eliminate the EC film pre-coating process, and thereby streamline the device structure and fabrication process. More importantly, the metal electrodeposition reactions enable much broader transmittance modulating range and larger modulating amplitude (from ~0.01% to 80–90%), thanks to the metals' high extinction coefficients in wide wavelength ranges.[11,18,19] However, metal electrodepositions are always plagued by the notorious "tip discharge effect" that instigates unstable dendritic deposition and an uneven coloring process.[11] Furthermore, the deposited dendrites may break at their roots in the dissolution (*i.e.*, bleaching) processes, and transform into dormant metal debris that lose electrical contact with the conductive substrates,

[a]*School of Environment and Materials Engineering, Yantai University, Yantai 264005, China. E-mail: fyjiang@ytu.edu.cn; kanglitao@ytu.edu.cn*

[b]*School of Chemistry & Chemical Engineering, Yantai University, Yantai 264005, China. E-mail: xiaoboy8@gmail.com*

[c]*Jiangsu Key Laboratory of Electrochemical Energy Storage Technologies, College of Materials Science and Technology, Nanjing University of Aeronautics and Astronautics, Nanjing 210016, China*

† F. J. Meng and J. S. Zhong contributed equally to this paper and are co-first authors

undermining the color switching amplitude and durability.[20] Decorating the substrates with Pt nanoparticles can guide uniform nucleation and growth of the deposited metals,[21,22] but at the expense of high preparation cost and complexity. Furthermore, parasitic reactions, such as corrosion and the resulting surface passivation, are also substantial challenges hindering the achievement of durable metal deposition EC systems.[23,24]

To circumvent the problems associated with metal deposition, researchers have begun to explore novel EC systems based on reversible electrodeposition/dissolution of nonmetallic materials. For instance, we[25] and Wang *et al.*[26] independently pioneered a corrosion-/dendrite-free MnO_2 electrodeposition EC system with the assistance of an acidized electrolyte ($Mn^{2+} + H_2O \leftrightarrow MnO_2 + 4H^+ + 2e^-$), achieving more than two times higher transmittance modulation amplitude compared with the conventional ion insertion/extraction color switching mechanism. Thanks to the electric insulation of MnO_2, the randomly formed MnO_2 protrusions will not enhance local electrical fields and abet dendrite growth, but instead self-limitingly passivate the deposited areas, enabling a highly uniform dendrite-free deposition process.[25] Furthermore, the high affinity between the deposited MnO_2 and the ITO/FTO substrates makes the Pt nanoparticle decoration process unnecessary.[26] To avoid the formation/accumulation of deposit debris, the electrolyte was further modified with Fe^{3+} as an electrochemically-active catalyst, which can facilitate the dissolution of MnO_2 after being electrochemically reduced into Fe^{2+}, resulting in much improved color switching durability.[25,27] Recently, Jia *et al.* further established an ultra-simple EC window featuring electrode-free structures and super-long durability, by coupling the MnO_2/Mn^{2+} and Cu^{2+}/Cu couples into one acidized electrolyte.[28]

In this paper, we report another nonmetallic electrodeposition/dissolution EC system based on the I^0/I^- couple. During the coloration process, the colorless I^- in the electrolyte is electrochemically oxidized to a brown I^0 species (*e.g.*, I_2, I_3^-, *etc.*), delivering a profound color change from colorless to deep brown. During bleaching, the I^0 species are reduced to I^-, driving the working electrode back to colorless transparent. This direct electron-transfer reaction ($2I^- - 2e^- \leftrightarrow I_2$; $3I^- - 2e^- \leftrightarrow I_3^-$) ensures fast color switching speed, thanks to their fast reaction kinetics. However, the polyiodide intermediate products, such as I_3^-, can easily dissolve into the electrolyte and shuttle to the counter electrode, leading to serious self-discharge and color fading.[29] Therefore, we further modify the electrolyte with an ionic liquid [EMIM]Cl (*i.e.*, 1-ethyl-3-methylimidazolium chloride). This electrolyte additive can effectively suppress polyiodide dissolution and shuttling by interacting with polyiodides and forming the insoluble $[EMIM]^+I_3^-$ coordination compound, significantly improving the color switching durability and optical memory performance. Thanks to the rational design, the EC system achieves state-of-the-art performance, including high optical modulation amplitude (89.6% at 500 nm), short response time ($t_{coloring}$: 7 s, $t_{bleaching}$: 6 s), and ultra-long cycling durability with the EC performance remaining almost unchanged within 10 000 color switching cycles.

2. Methods

2.1 Electrolytes

Zinc sulfate ($ZnSO_4 \cdot 7H_2O$, Aladdin Co. Ltd, 99.5%) and potassium iodide (KI, Aladdin Co. Ltd, 99%) was dissolved into the 50 mL deionized water (DI water) to obtain the 24.23 g $ZnSO_4$–0.83 g KI control electrolyte. The modified electrolyte was prepared by adding 1.46 g of 1-ethyl-3-methylimidazolium chloride ($C_6H_{11}ClN_2$, Aladdin, 98%, [EMIM]Cl) into the control electrolyte. To simplify the discussion, the 24.23 g $ZnSO_4$–0.83 g KI control electrolyte and the 24.23 g $ZnSO_4$–0.83 g KI–1.46 g [EMIM]Cl modified electrolyte are labeled as ZIE and ZI electrolyte, respectively.

2.2 Assembly of the electrochromic devices

The EC devices were assembled with FTO glass ($\sim$10 Ω sq^{-1}, 2.5 $\times$ 3.0 $\times$ 2.2 mm, Shangyang Co. Ltd) as the working electrode, and a narrow Zn foil belt (0.1 mm thick, Saibo Co. Ltd) attached onto a flat glass electrode as the counter electrode. These two glasses were adhered and separated by 1-mm-thick double-sided tape (5 mm wide, 3M Company Co. Ltd), forming hollow double-paned EC devices. Afterwards, the ZIE electrolyte was injected into the internal cavities of these devices using a syringe. Then, the edges of the device were further sealed with silicone adhesive to avoid electrolyte leakage. To ensure good electrical contact between the electrodes and the external circuit, Cu conductive adhesive foil tape (0.06 mm thick and 5 mm wide, Maoye Co. Ltd) was tightly pasted to the margins of these electrodes. Zn||Zn symmetrical cells were fabricated by coupling two Zn plates (thickness: 100 μm, Φ = 16 mm) in a coin cell filled with 120 μL electrolyte.

2.3 Material characterization

The surficial morphologies and elemental mapping images of the samples were characterized by using a JEOL JSM-7610F field emission scanning electron microscope (SEM) equipped with an energy-dispersive spectroscope (EDS). For *in situ* observation, a home-made transparent device was fabricated by immersing an FTO glass working electrode and a zinc foil counter electrode into a 1.0 $\times$ 2.3 cm^2 transparent quartz cuvette filled with electrolyte (Fig. S1). The optical properties and morphological changes of the working electrode during the bleaching and coloration processes were measured by a Persee TU-1810 UV-visible spectrophotometer and JT-H360-B optical microscope, respectively. FTIR-ATR (Fourier transform Infrared-Attenuated Total Reflectance) spectra were collected on a Nicolet iN10 spectrometer within a wavenumber range of 400–4000 cm^{-1}. X-ray photoelectron spectra (XPS) were recorded on a Thermo Scientific K-Alpha™⁺ spectrometer to analyze the chemical state of the imidazole before and after I_3^- adsorption.

2.4 Density functional theory (DFT) calculations

All the calculations were carried out by using the VASP package.[30,31] The cutoff energy was set to be 520 eV. The electron–ion interactions were described by using projector augmented wave,[32] and the Perdew–Burke–Ernzerhof version of the generalized gradient approximation was used for the exchange and correlation functionals.[33] For the structure relaxations, the *k*-points were set to be $1 \times 1 \times 1$ in view of the isolated system considered in this work. The convergence threshold for the structure relaxation was set to be 0.02 eV $Å^{-1}$ in force and 10^{-4} eV in energy. The spin polarization was considered in the calculations.

2.5 Electrochemical and optical characterization

Optical tests were performed on a Persee TU-1810 UV-visible spectrophotometer, with a quartz cuvette filled with the electrolyte as the baseline. To investigate the EC performance and cycling durability, a CHI-660E electrochemical workstation was used to impose controlled voltages to the FTO working electrode. Electrochemical tests of the FTO glass working electrode and the EC device were performed in a two-electrode configuration, with Zn foil as both the counter and reference electrode (Fig. S1). CV (cyclic voltammetry), potentiation current–time transient, CP (chronopotentiometry) and LSV (linear sweep voltammetry) curves of the Zn counter electrodes were also collected on the CHI-660E electrochemical workstation.

3. Results and discussion

Fig. 1a and b compare the cyclic voltammetry (CV) curves and optical photographs of the two FTO glass electrodes separately working in the ZI and ZIE electrolyte. In both electrolytes, the CV curves demonstrate a pair of well-defined redox peaks, indicating the occurrence of a reversible I^0/I^- conversion reaction (Fig. S2 and 1c).[34] During the anodic processes, the generated I^0 species tinted the working electrodes brown, because of their strong absorption of green light.[35,36] In the cathodic processes, the I^0 species were reduced back to colorless I^-, and the electrodes returned colorless transparent again. However, the color change in the ZI electrolyte was much shallower than that in the ZIE electrolyte. At the same time, the

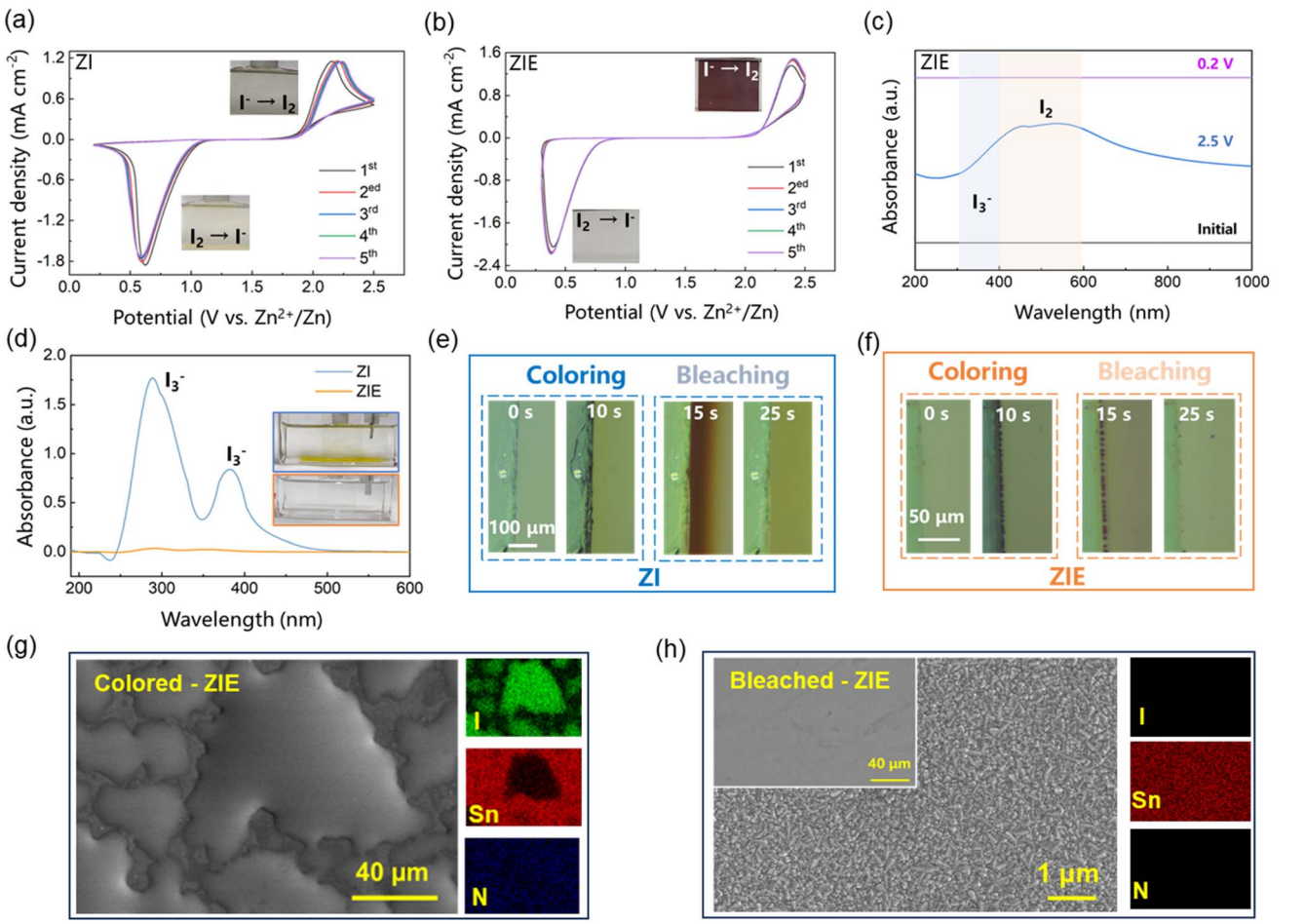

Fig. 1 Iodine electrodeposition behavior onto FTO glass working electrodes in different electrolytes: (a and b) CV curves at 10 mV s^{-1} and optical photographs in their bleached and colored state, (c) absorption spectra of the electrode at different voltages in the ZIE electrolyte; (d) absorbance spectra of the cycled electrolytes; (e and f) *in situ* optical microscopy observation showing the iodine electrodeposition process in different electrolytes; (g and h) SEM and elemental mapping images of the colored and bleached electrodes in the ZIE electrolyte.

CV peaks collected in the ZI electrolyte gradually shrank during the cycling test, while the polarization potentials between the anodic and cathodic peaks increased, suggesting an inferior reaction reversibility. The reaction irreversibility can be ascribed to the formation and dissolution of the I_3^- intermediate ($I_2 + I^- \leftrightarrow I_3^-$; $3I^- - 2e^- \leftrightarrow I_3^-$, Fig. S2). It is difficult to completely reduce the dissolved I_3^- in the electrolyte back to I^- within the limited bleaching times, because of its electric disconnection with the working electrodes.[37] As a result, a considerable amount of I_3^- remained in the ZI electrolyte after the tests (Fig. 1d and e). In contrast, the CV curves collected in the ZIE electrolyte enlarged in the 2nd cycle, and kept highly stable afterwards in both shape and position (Fig. 1b). After the test, the cycled ZIE electrolyte remained colorless, transparent and I_3^- free (Fig. 1d), indicating a significantly-improved reaction reversibility thanks to the vanishment of the I_3^- intermediate in this medium (Fig. 1c).

The suppression of I_3^- formation by the ZIE electrolyte has also been confirmed by *in situ* optical microscopy observation (Fig. 1e and f). In the ZI electrolyte, the deposited I^0 species on the electrode's surface gradually dissolved and diffused into the electrolyte (Fig. 1e and S3). After the reaction, a considerable proportion of the dissolved I^0 species remained in the electrolyte. In the ZIE electrolyte, on the other hand, the I^0 species deposited onto the working electrode in the form of a uniform insoluble layer (Fig. 1f and S4). As time went on, the layer became thicker, indicating that one can easily control the color depth of the electrode by simply changing the voltage application time. During the dissolution (bleaching) process, the layer was gradually stripped and transformed into disconnected droplets, and then totally vanished, characterizing the complete conversion of I^0 species into soluble I^-. Fig. S5, 1g and h depict the SEM and elemental mapping images of the initial, colored and bleached FTO electrodes working in the ZIE electrolyte, respectively. The initial FTO film consisted of tightly packed grains that ensure both high optical transmittance and electrical conductivity (Fig. S5). In the colored state, a droplet-shaped compound containing both I and N elements appeared on the electrode's surface (Fig. 1g), suggesting the successful deposition of iodine species (*e.g.*, I_2 and $[EMIM]^+I_3^-$, Fig. 1c). After bleaching at 0.2 V, all the deposits were completely removed, confirming again the high reversibility of the I^0/I^- conversion reaction in the modified ZIE electrolyte (Fig. 1h). The sharp variation of the N content accompanied with the iodine deposition/dissolution clearly demonstrates that the [EMIM]Cl additive played a crucial role in suppressing I_3^- formation and improving I^0/I^- conversion reversibility (Table S1).

To investigate the detailed working mechanism of this additive, we prepared two identical I_3^- solutions, and added [EMIM]Cl additive into one of the solutions. The solution became cloudy and deeper brownish immediately after adding the [EMIM]Cl (Fig. 2a). After 2 hours, the cloudy suspension separated into a deep brown participation layer at the bottom of the solution, and a light brown supernatant with much less I_3^- above (Fig. 2a). This result indicates that the contact of $[EMIM]^+$ and I_3^- leads to the formation of an insoluble product with a much deeper color, which can thereby restrain polyiodide shuttling and improve the I^0/I^- conversion kinetics as well as optical contrast. To further clarify the interaction, the adsorption energies between imidazole and different iodide species were calculated by using first-principles simulations. As shown

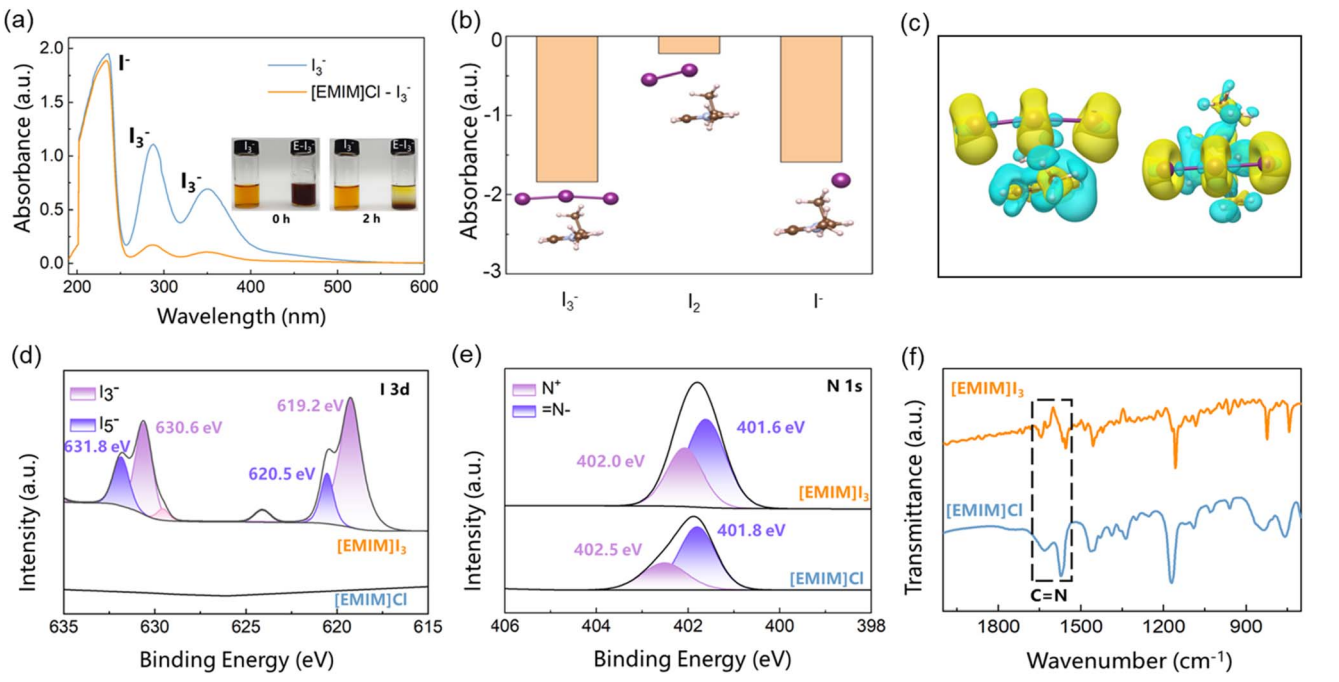

Fig. 2 Studies on the interactions between $[EMIM]^+$ and iodine species: (a) absorbance spectra and photographs showing the coordination between I_3^- and $[EMIM]^+$; (b) the calculated adsorption energies of I_2, I_3^-, and I^- on $[EMIM]^+$; (c) the calculated charge density differences with I_3^- and $[EMIM]^+$; (d and e) the high-resolution XPS and (f) FTIR test of [EMIM]Cl and $[EMIM]I_3$.

in Fig. 2b, the calculated adsorption energy between $[EMIM]^+$ and I_3^- (−1.84 eV) is much higher than those with I^- (−1.59 eV) and I_2 (−0.22 eV), indicating that the coordination between $[EMIM]^+$ and I_3^- is energetically preferential. The corresponding charge density difference between $[EMIM]^+$ and I_3^- is shown in Fig. 2c, in which the yellow and cyan colors represent the charge accumulation and depletion regions, respectively. The Bader charge analysis revealed that N atoms in the $[EMIM]^+$ cation initially had 2.38 electrons, while after the adsorption of I_3^-, the N atoms obtained additional 0.04 electrons. It is noted that there are also some charge accumulation regions (yellow colors) within the $[EMIM]^+$, which means that the adsorption of I_3^- will induce electron redistribution in the whole $[EMIM]^+$. The electron transfer and redistribution between $[EMIM]^+$ and I_3^- were further investigated by collecting the X-ray photoelectron spectra (XPS) of the [EMIM]Cl additive and the $[EMIM]I_3$ precipitation. As shown in Fig. 2d, S6 and S7, the [EMIM]Cl is iodide-free and shows no peaks from iodine species. In contrast, obvious I 3d peaks appear in the XPS spectrum of the $[EMIM]I_3$, which can be deconvoluted into pairs of sub-peaks from I_3^- and I_5^- anions.[38,39] At the same time, both the N 1s peaks, especially the N^+ one, shift to the lower binding energy direction after the coordination with I_3^- (Fig. 2e).[40–42] This observation demonstrates that the iodine species imparted partial charges to the N atoms of $[EMIM]^+$, in good line with the calculation results.[43] Fig. 2f further exhibits the FTIR spectra of these samples. Compared with [EMIM]Cl, the C=N vibration peaks of $[EMIM]I_3$ shift to a lower wavenumber (from 1633, 1573 to 1623, 1555 cm^{-1}, respectively),[44,45] confirming again the interactions between the N-based functional groups and the I_3^-. The strong interaction converted the dissolved I_3^- into $[EMIM]I_3$ precipitation, thereby suppressing the polyiodide shuttling. It should be noted that the $[EMIM]I_3$ complex is still highly electrochemically active after deposition.[46] This means that the deposited $[EMIM]I_3$ can be readily reduced back to $[EMIM]^+$ cations and I^- anions, and released back to the electrolyte again during the bleaching processes. The high $[EMIM]I_3$ deposition/dissolution reversibility endows this additive with a long-term effectiveness.

Fig. 3 shows the transmittance spectra and photographs of the colored-/bleached-FTO working electrode in the ZIE electrolyte. In the bleached state, the electrode is colorless transparent, thanks to the high transmittance of the FTO substrate and the ZIE electrolyte. In the colored state, the electrode became deep brown, because of the deposition of tinting I^0 species.[35,36] The thickness of the deposition layer and thus the color depth of the electrode can be easily controlled by simply changing the voltage application time (Fig. S8). After only 10 s, the electrode achieved a very high transmittance modulation amplitude of up to 89.6% at 500 nm (Fig. 3a). However, the transmittance change was obviously shallower and slower without $[EMIM]^+$ being involved (28.4%, Fig. S9, S10a and c), due to the dissolution and shuttling of I_3^-. The backlog of I_3^- in the ZI electrolyte restricted not only the coloring depth, but also the overall transmittances of the system during the cycling test, regardless of the color state (Fig. S10b). In contrast, the addition

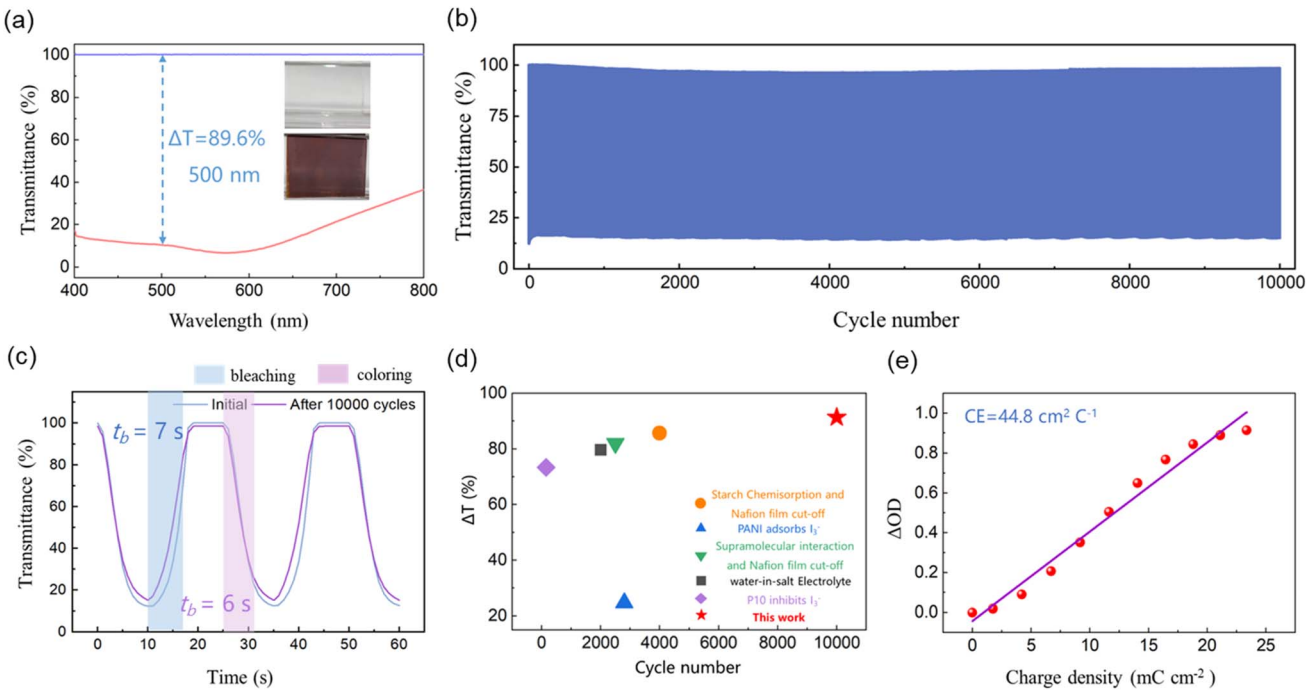

Fig. 3 EC performance of the I^0/I^- conversion system in the ZIE electrolyte: (a) transmittance spectra and photographs in the bleached and colored state; (b) cycling performance within 10 000 cycles; (c) transmittance evolution curves showing the color switching speeds and transmittance modulation amplitude in the initial and final cycles; (d) performance comparison between this work and reported iodine-related EC systems; (e) linear fitting result of the optical density variation (ΔOD, @500 nm) *vs.* charge density curve that determines the coloration efficiency.

of $[EMIM]^+$ enables an excellent cycling durability, with the optical modulation ability and switching speed keeping almost unchanged within 10 000 continuous color switching cycles (Fig. 3b, c and S11), the best reported value to date (Fig. 3d and Table S2). Thanks to the improvement of the reaction kinetics and reversibility, the electrode also delivered a higher coloring efficiency in the ZIE electrolyte (44.8 *vs.* 6.1 $cm^2\ C^{-1}$, Fig. 3e and S10d), indicating that the same amount of charge insertion can trigger profounder optical modulations. The comprehensively improved performance achieved in the ZIE electrolyte highlights again the critical contribution of the [EMIM]Cl additive. Moreover, the research by Zhong *et al.* suggests that it is possible to further enhance the electrochromic performance of the system by tailoring the anions.[47]

In practical EC devices, in order to keep the overall charge balance, counter electrodes are usually needed to synchronously compensate for the charge/ion fluctuation caused by the EC reactions.[48] Metallic Zn simultaneously exhibits high electrical conductivity, high electrochemical activity, and high theoretical capacity (up to 5855 mAh cm^{-3}), and therefore is regarded as a suitable counter electrode candidate for many EC devices.[49] However, Zn electrodes often seriously suffer from dendrite growth, corrosion and surface passivation during cyclic electrochemical deposition/stripping.[50] As shown in Fig. 4a and S12, the Zn foil was seriously corroded after 7 days of soaking in the ZI electrolyte. In EC devices, these detrimental parasitic reactions not only slow down the color switching speeds, but also degrade the optical contrast and shorten the service life.[16] The addition of [EMIM]Cl can effectively suppress Zn corrosion (Fig. 4b and S12), since $[EMIM]^+$ can be preferentially adsorbed onto the Zn surface.[46] As shown in Fig. 4c, the Zn corrosion current in the ZIE electrolyte was nearly 5 times lower than that in the ZI electrolyte (0.307 *vs.* 1.438 mA cm^{-2}), while the corrosion potential was 8 mV higher (−15 *vs.* −23 mV, Fig. 4c), confirming the excellent corrosion resistance of the Zn foils in the ZIE electrolyte.[51] LSV tests further suggest that the addition of [EMIM]Cl can also retard the H_2 evolution reaction and widen the stable voltage window of the electrolyte (Fig. 4d). Due to the suppression of the parasitic reactions, Zn electrodeposition was much more stable in the modified ZIE

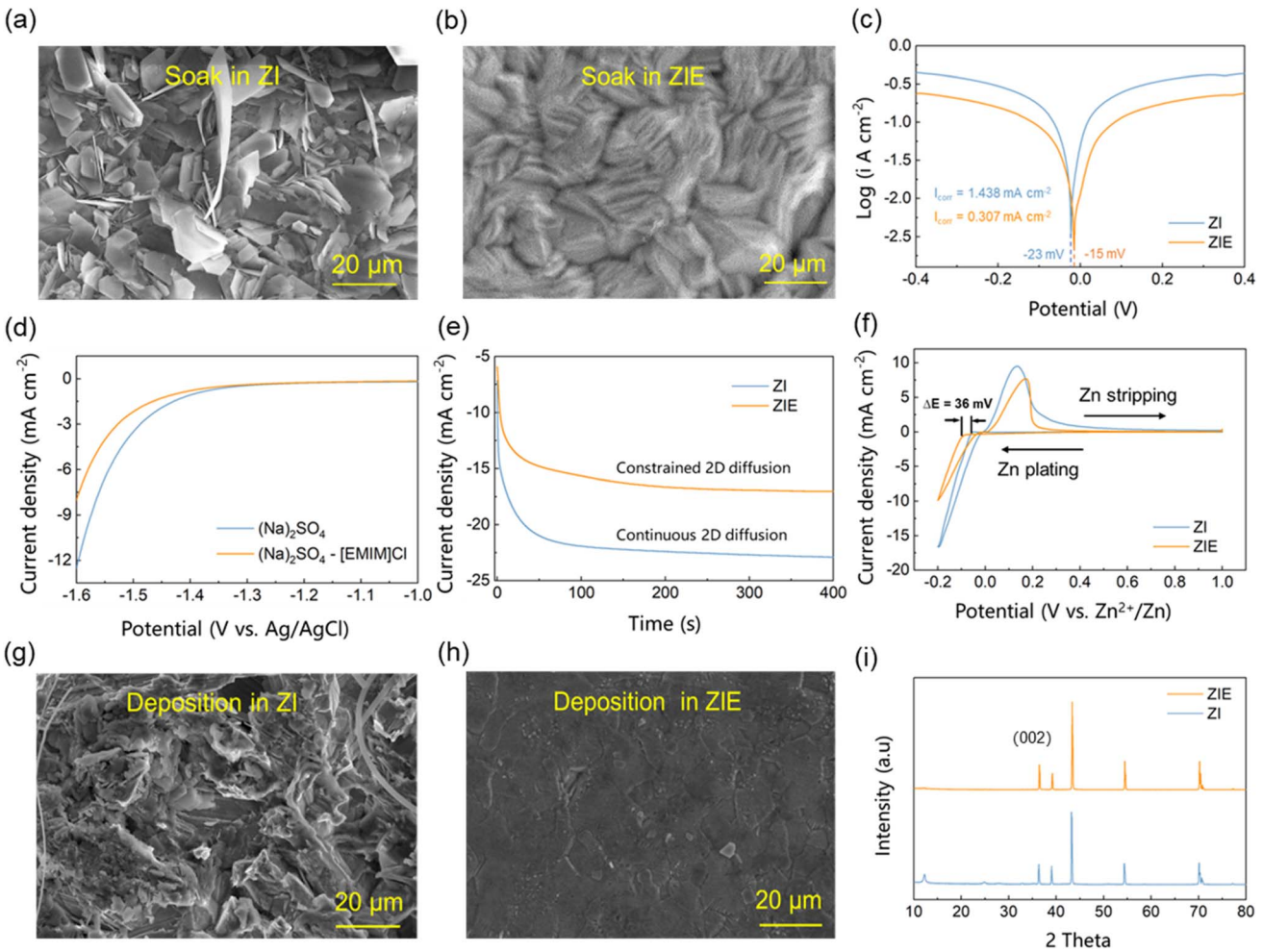

Fig. 4 Influence of the [EMIM]Cl additive on the electrochemical stability of the Zn counter electrode: (a and b) SEM images of the Zn foils soaked in the ZI and ZIE electrolyte after 7 days; (c) Tafel plots; (d) LSV curves; (e) chronoamperometry tests; (f) CV curves for Zn deposition/stripping on Ti foils; (g and h) SEM images of Zn foils after 30 cycles in the ZI and ZIE electrolyte at 2.5 mA cm^{-2} and 2.5 mAh cm^{-2}; (i) XRD patterns of the cycled Zn foil electrodes.

electrolyte (Fig. 4e). In contrast, the Zn deposition current density in the ZI electrolyte experienced a sustained increase, signaling a persistent and rampant growth of dendrites.[52,53] Fig. 4f shows the CV curves of the Zn||Ti asymmetric cells that can be used to analyze the nucleation and growth process of the deposited Zn.[54] The cell exhibited 36 mV higher nucleation overpotential in the ZIE electrolyte, which led to smaller nuclei sizes and compact deposition.[55] As shown in Fig. 4g, the Zn deposits in the ZI control electrolyte were disordered and uneven. In the ZIE electrolyte, on the other hand, the deposit layer was not only flatter and denser (Fig. 4h), but also contained less byproduct (Fig. 4i). As expected, the modified Zn deposition behavior and suppressed parasitic reactions significantly enhanced the cycling durability of the Zn electrode. Tested at 2.5 mA cm^{-2} and 2.5 mAh cm^{-2}, the Zn||Zn symmetrical cells worked properly for 337 h in the ZIE electrolyte, whereas the ZI electrolyte cell failed after only 100 h (Fig. S13). These results indicate that the addition of [EMIM]Cl is beneficial to improving the cycling stability of both the iodine and Zn electrode.

Inspired by the multifaceted merits of the ZIE electrolyte, an EC device was assembled with an FTO glass working electrode, a metallic Zn counter electrode and a suitable amount of the electrolyte, in order to demonstrate the potential application of this EC system. The working mechanism of this device is graphically illustrated in Fig. 5a. During the coloration process, I^- in the electrolyte is oxidized into I^0 species (*i.e.*, I_2 and $[EMIM]I_3$) and deposited on to the surface of the FTO electrode. To keep the overall charge balance, Zn^{2+} in the electrolyte is reduced into metallic Zn and deposited onto the Zn counter

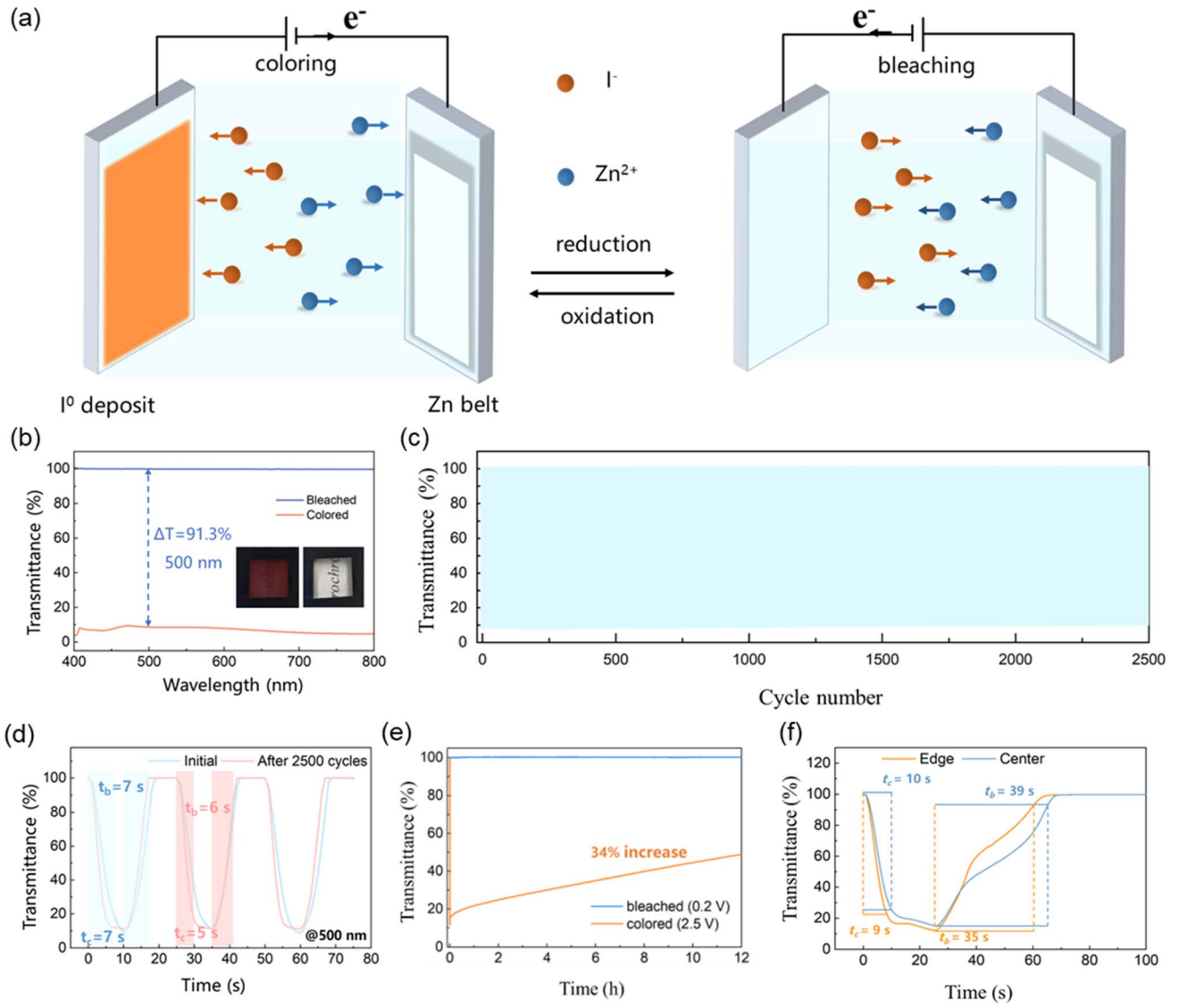

Fig. 5 Characterizations of the I_2–Zn EC device: (a) schematic diagrams showing the device's working principle; (b) transmittance spectra and photographs in its bleached and colored state; (c) cycling performance test; (d) transmittance evolution curves showing the color switching speeds and transmittance modulation amplitude in the initial and final cycles; (e) optical memory performance during open-circuit rest; (f) transmittance evolution curves measured at the edge and center of a large-area (10 × 10 cm^2) device.

electrode.[56,57] Since both electrodes are highly reversible, manipulating the stimulating voltage can effectively control the extent of the reactions and drive the device to the target color state (Fig. S14).[58,59] In this device, the color switching enabled a noteworthy optical modulation of 91.3% at 500 nm (between 8.7% and 100%, Fig. 5b), which kept constantly stable within the 2500-times testing cycles, an outstanding level in water-based electrolyte electrochromic devices (Fig. 5c and Table S3). The shorter lifetime of the device than the electrolytic cell (Fig. 3b and 5c) can be primarily attributed to the high iodine adsorption capacity of the 3M double-sided tape (Fig. S15a). In the failed device, the 3M tape had adsorbed the majority of the iodine, and thereby caused electrochromic performance degradation by depleting the available active substance. By replacing fresh electrolyte, the electrochromic performance of the device could be completely restored (Fig. S15b). This finding reminds us to consider the potential impact of encapsulation materials on the longevity and performance of electrochromic devices.

Transmittance evolution curves indicate that the incorporation of a Zn counter electrode did not slow down the color switching speeds. In fact, the $t_{bleaching}$ and $t_{coloring}$ of the device slightly decrease from 7/7 s to 6/5 s after 2500 cycles, respectively (Fig. 5d), probably due to the activation of the electrode/electrolyte interface and the reduction in the interface impedance (Fig. S16). Furthermore, this device manifested also a decent optical memory ability, because the polyiodide shuttling process had been effectively suppressed by the [EMIM]Cl additive. After 12 h of open-circuit rest, the colored-state transmittance increased by 34%, while the bleached-state transmittance remained constant. This means that the majority of color contrast (~65%) can be reserved after 12 h, a time long enough to cover the entire sunshine duration of a day (Fig. 5e). To show the scaling potential of this EC system, we further fabricated a 10 × 10 cm^2 area device and evaluated its EC properties. The device achieved profound transmittance variation of 84.9% ~86.8% at 500 nm (Fig. S17 and S18). The fast and similar response times at the center and edge demonstrate its uniform coloration processes and practicality for smart window applications (Fig. 5f).

4. Conclusion

In this paper, a dendrite- and corrosion-free nonmetallic electrodeposition EC system is established based on the I^0/I^- conversion, achieving fast and reversible color switching between colorless transparent and deep brown. The experimental results show that suppressing I_3^- formation and dissolution is crucial to improving the reaction kinetics and reversibility. Therefore, an electrolyte modifying method is further developed with [EMIM]Cl as the additive. In the modified electrolyte, the dissociated $[EMIM]^+$ can coordinate with I_3^- and form insoluble $[EMIM]I_3$ with deeper color, and therefore effectively suppress the polyiodide shuttling issues. With this merit, the iodine electrodeposition system delivers a high transmittance modulation amplitude up to 89.6% and excellent cycling durability without performance degradation within 10 000 cycles. Furthermore, the dissociated $[EMIM]^+$ can also preferentially adsorb onto the Zn counter electrodes, and thereby slow down detrimental dendrite growth and corrosion. Finally, the application potential of this system is systematically demonstrated by constructing high performance I_2–Zn full EC devices, providing an innovative avenue for the development of novel EC systems.

Author contributions

All authors have accepted responsibility for the entire content of this manuscript and approved its submission. Fengjiao Meng: methodology, formal analysis, writing – original draft. Junsen Zhong: conceptualization, validation, writing – original draft. Xiaoqian Tan: data curation, formal analysis. Jianbo Cheng: software. Bo Xiao: software, formal analysis, investigation, visualization. Shengliang Zhang: resources. Fuyi Jiang: supervision, resources. Wenbao Liu: resources. Wei Liu: funding acquisition, resources. Litao Kang: methodology, project administration, supervision, writing – review & editing, funding acquisition, resources.

Conflicts of interest

There are no conflicts to declare.

Data availability

All the data used to support the findings of this study can be made available by the corresponding authors upon request.

Supplementary information is available. See DOI: **https://doi.org/10.1039/d5sc04767f**.

Acknowledgements

The authors thank the National Natural Science Foundation of China (52072328, 22327807, 62105148, 52201280), the Shandong Provincial Natural Science Foundation (ZR2025MS957, ZR2021QB200), and the Open Foundation of Key Laboratory for Palygorskite Science Applied Technology of Jiangsu Province (HPK202103) for financial support.

References

1 Y. Huang, *et al.*, Electrochromic Materials Based on Ions Insertion and Extraction, *Adv. Opt. Mater.*, 2022, **10**(4), 2101783.
2 M. Li, *et al.*, Manipulating metals for adaptive thermal camouflage, *Sci. Adv.*, 2020, **6**(22), eaba3494.
3 B. Wang, *et al.*, A Long-Life Battery-Type Electrochromic Window with Remarkable Energy Storage Ability, *Sol. RRL*, 2020, **4**(3), 1900425.
4 E. Syrrakou, S. Papaefthimiou and P. Yianoulis, Environmental assessment of electrochromic glazing production, *Sol. Energy Mater. Sol. Cells*, 2005, **85**(2), 205–240.

5 Z. Shao, *et al.*, All-solid-state proton-based tandem structures for fast-switching electrochromic devices, *Nat. Electron.*, 2022, **5**(1), 45–52.
6 D. Zhuang, *et al.*, Amorphous Hydrated Tungsten Oxides with Enhanced Pseudocapacitive Contribution for Aqueous Zinc-Ion Electrochromic Energy Storage, *Adv. Energy Mater.*, 2024, **14**(40), 2402603.
7 H. Li, *et al.*, Ultrafast, Stable Electrochromics Enabled by Hierarchical Assembly of V_2O_5@C Microrod Network, *ACS Appl. Mater. Interfaces*, 2022, **14**(42), 48037–48044.
8 R. Liu, *et al.*, Organic Ligand-Free Scalable Dual-Band Electrochromic Smart Windows, *Adv. Funct. Mater.*, 2025, **35**(1), 2409914.
9 B. Huang, *et al.*, Prolonging lifespan of Prussian blue electrochromic films by an acid-free bulky-anion potassium organic electrolyte, *Chem. Eng. J.*, 2022, **449**, 137850.
10 W. Wu, *et al.*, Boosting Transport Kinetics of Ions and Electrons Simultaneously by Ti_3C_2Tx (MXene) Addition for Enhanced Electrochromic Performance, *Nano-Micro Lett.*, 2020, **13**(1), 20.
11 M. T. Strand, *et al.*, Polymer inhibitors enable >900 cm^2 dynamic windows based on reversible metal electrodeposition with high solar modulation, *Nat. Energy*, 2021, **6**(5), 546–554.
12 R.-T. Wen, C. G. Granqvist and G. A. Niklasson, Eliminating degradation and uncovering ion-trapping dynamics in electrochromic WO_3 thin films, *Nat. Mater.*, 2015, **14**(10), 996–1001.
13 D. Dong, *et al.*, Life-cycling and uncovering cation-trapping evidence of a monolithic inorganic electrochromic device: glass/ITO/WO_3/$LiTaO_3$/NiO/ITO, *Nanoscale*, 2018, **10**(35), 16521–16530.
14 T. S. Hernandez, *et al.*, Bistable Black Electrochromic Windows Based on the Reversible Metal Electrodeposition of Bi and Cu, *ACS Energy Lett.*, 2018, **3**(1), 104–111.
15 A. L.-S. Eh, *et al.*, Robust Trioptical-State Electrochromic Energy Storage Device Enabled by Reversible Metal Electrodeposition, *ACS Energy Lett.*, 2021, **6**(12), 4328–4335.
16 B. Huang, *et al.*, A Dual-Mode Anode-Free Zinc-Prussian Blue Electrochromic Device, *Adv. Funct. Mater.*, 2025, 2423532.
17 L. Wang, *et al.*, A Solar Water-Heating Smart Window by Integration of the Water Flow System and the Electrochromic Window Based on Reversible Metal Electrodeposition, *Adv. Sci.*, 2022, **9**(6), 2104121.
18 C. Park, *et al.*, Transparent Electrochemical Gratings from a Patterned Bistable Silver Mirror, *ACS Nano*, 2017, **11**(7), 6977–6984.
19 C. J. Barile, *et al.*, Dynamic Windows with Neutral Color, High Contrast, and Excellent Durability Using Reversible Metal Electrodeposition, *Joule*, 2017, **1**(1), 133–145.
20 X. Liu, *et al.*, Stabilizing Nickel–Copper Co-Deposition Electrochromism with the Assistance of Bromine Redox, *Inorg. Chem.*, 2025, **64**(2), 1016–1022.
21 S. M. Islam, *et al.*, Hybrid dynamic windows using reversible metal electrodeposition and ion insertion, *Nat. Energy*, 2019, **4**(3), 223–229.
22 M. Cui, *et al.*, Quasi-Isolated Au Particles as Heterogeneous Seeds To Guide Uniform Zn Deposition for Aqueous Zinc-Ion Batteries, *ACS Appl. Energy Mater.*, 2019, **2**(9), 6490–6496.
23 S. M. Islam and C. J. Barile, Dynamic Windows Using Reversible Zinc Electrodeposition in Neutral Electrolytes with High Opacity and Excellent Resting Stability, *Adv. Energy Mater.*, 2021, **11**(22), 2100417.
24 B. Xu, *et al.*, The Progress and Outlook of Multivalent-Ion-Based Electrochromism, *Small Sci.*, 2023, **3**(11), 2300025.
25 X. Liu, Visible light electrochromism based on reversible dissolution/deposition of MnO_2, *Nanophotonics*, 2024, **13**, 679–686.
26 J. Wang, *et al.*, A Reversible MnO_2 Deposition-Enabled Multicolor Electrochromic Device with Efficient Tunability of Ultraviolet–Visible Light, *Small*, 2024, **20**(21), 2310229.
27 X. Zhang, *et al.*, Fast-Switching Electrochromic Device Enabled by Fe^{2+}-Mediated MnO_2/Mn^{2+} Redox Reactions, *ACS Appl. Electron. Mater.*, 2024, **6**(11), 8163–8170.
28 Z. Jia, *et al.*, Electrochromic windows with fast response and wide dynamic range for visible-light modulation without traditional electrodes, *Nat. Commun.*, 2024, **15**(1), 6110.
29 F. Meng, *et al.*, A high-capacity and self-healable electrochromic system based on I0/CuI conversion reaction, *Chem. Eng. J.*, 2024, **500**, 157375.
30 F. J. Kresse G, Efficiency of ab-initio total energy calculations for metals and semiconductors using a plane-wave basis set, *Comput. Mater. Sci.*, 1996, **6**(1), 15–50.
31 F. J. Kresse G, Efficient iterative schemes for ab initio total-energy calculations using a plane-wave basis set, *Phys. Rev. B: Condens. Matter Mater. Phys.*, 1996, **54**(16), 11169–11186.
32 G. Kresse and D. Joubert, From ultrasoft pseudopotentials to the projector augmented-wave method, *Phys. Rev. B: Condens. Matter Mater. Phys.*, 1999, **59**(3), 1758–1775.
33 Y. Wang and J. P. Perdew, Correlation hole of the spin-polarized electron gas, with exact small-wave-vector and high-density scaling, *Phys. Rev. B: Condens. Matter Mater. Phys.*, 1991, **44**(24), 13298–13307.
34 F. Meng, *et al.*, A high-capacity and self-healable electrochromic system based on I0/CuI conversion reaction, *Chem. Eng. J.*, 2024, **500**, 157375.
35 X. Liu, *et al.*, Cathode material design of static aqueous Zn-I_2 batteries, *J. Energy Storage*, 2024, **84**, 110765.
36 J. Ma, *et al.*, Iodine Redox Chemistry in Rechargeable Batteries, *Angew. Chem., Int. Ed.*, 2021, **60**(23), 12636–12647.
37 H. Chen, *et al.*, Aqueous Zinc-Iodine Batteries: From Electrochemistry to Energy Storage Mechanism, *Adv. Energy Mater.*, 2023, **13**(41), 2302187.
38 Z. Zhu, *et al.*, Long-life aqueous zinc-iodine batteries enabled by selective adsorption of polyiodide anions in nonporous adaptive organic cages, *Energy Storage Mater.*, 2025, **75**, 103994.
39 X. Liao, *et al.*, Cation Adsorption Engineering Enables Dual Stabilizations for Fast-Charging Zn–I_2 Batteries, *Adv. Energy Mater.*, 2024, **14**(47), 2402306.
40 X. Yang, J. Luo and X. Sun, Towards high-performance solid-state Li–S batteries: from fundamental understanding to engineering design, *Chem. Soc. Rev.*, 2020, **49**(7), 2140–2195.

41 T. Zhao, *et al.*, Nonflammable localized high-concentration deep eutectic electrolytes for safe and stable rechargeable aluminum batteries, *Nano Energy*, 2024, **131**, 110298.
42 Y.-X. Song, *et al.*, Polyaniline-vanadium oxide composite for Zn-ion electrochromic devices and mechanistic investigation by in-situ Raman spectroscopy, *Rare Met.*, 2025, **44**, 7700–7709.
43 J.-L. Yang, *et al.*, Janus Binder Chemistry for Synchronous Enhancement of Iodine Species Adsorption and Redox Kinetics toward Sustainable Aqueous Zn–I_2 Batteries, *J. Am. Chem. Soc.*, 2024, **146**(10), 6628–6637.
44 J. He, *et al.*, Synergistic effects of Lewis acid–base and Coulombic interactions for high-performance Zn–I2 batteries, *Energy Environ. Sci.*, 2024, **17**(1), 323–331.
45 H. Wu, *et al.*, Aqueous Zinc–Iodine Pouch Cells with Long Cycling Life and Low Self-Discharge, *J. Am. Chem. Soc.*, 2024, **146**(24), 16601–16608.
46 T. Xiao, *et al.*, All-Round Ionic Liquids for Shuttle-Free Zinc-Iodine Battery, *Angew. Chem., Int. Ed.*, 2024, **63**(8), e202318470.
47 W. Zhong, *et al.*, Cation-driven phase transition and anion-enhanced kinetics for high energy efficiency zinc-interhalide complex batteries, *Nat. Commun.*, 2025, **16**(1), 4586.
48 C. Gu, *et al.*, Emerging Electrochromic Materials and Devices for Future Displays, *Chem. Rev.*, 2022, **122**(18), 14679–14721.
49 X. Yang, Synchronous Dual Electrolyte Additive Sustains Zn Metal Anode with 5600, *Angew. Chem., Int. Ed.*, 2023, **62**, e202218454.
50 J. Bu, *et al.*, Interfacial Adsorption Layers Based on Amino Acid Analogues to Enable Dual Stabilization toward Long-Life Aqueous Zinc Iodine Batteries, *Adv. Mater.*, 2025, 2420221.
51 J. Feng, *et al.*, Regulating Zn2+ Migration-Diffusion Behavior by Spontaneous Cascade Optimization Strategy for Long-Life and Low N/P Ratio Zinc Ion Batteries, *Angew. Chem., Int. Ed.*, 2024, **63**(41), e202407194.
52 Z. Yang, *et al.*, Revealing the Two-Dimensional Surface Diffusion Mechanism for Zinc Dendrite Formation on Zinc Anode, *Small*, 2022, **18**(43), 2104148.
53 H. Zhang, *et al.*, Inducing the Preferential Growth of Zn (002) Plane for Long Cycle Aqueous Zn-Ion Batteries, *Adv. Energy Mater.*, 2023, **13**(1), 2203254.
54 H. Lu, *et al.*, Amino Acid-Induced Interface Charge Engineering Enables Highly Reversible Zn Anode, *Adv. Funct. Mater.*, 2021, **31**(45), 2103514.
55 M. Liu, *et al.*, Nanoscale Ultrafine Zinc Metal Anodes for High Stability Aqueous Zinc Ion Batteries, *Nano Lett.*, 2023, **23**(2), 541–549.
56 B. Wang, *et al.*, A Long-Life Battery-Type Electrochromic Window with Remarkable Energy Storage Ability, *Sol. RRL*, 2020, **4**(3), 1900425.
57 L. Kang, *et al.*, Rechargeable Aqueous Zinc-Ion Batteries with Mild Electrolytes: A Comprehensive Review, *Batteries Supercaps*, 2020, **3**(10), 966–1005.
58 H. Li, C. J. Firby and A. Y. Elezzabi, Rechargeable Aqueous Hybrid Zn^{2+}/Al^{3+} Electrochromic Batteries, *Joule*, 2019, **3**(9), 2268–2278.
59 W. Wu, *et al.*, Electrochromic devices constructed with water-in-salt electrolyte enabling energy-saving and prolonged optical memory effect, *Chem. Eng. J.*, 2022, **446**, 137122.